Feasibility of breast cancer lesion detection using a multi-frequency trans-admittance scanner (TAS) with 10 Hz to 500 kHz bandwidth

Tong In Oh[1]**, Jeehyun Lee**[2]**, Jin Keun Seo**[2]**, Sung Wan Kim**[2] **and Eung Je Woo**[1]

[1] College of Electronics and Information, Kyung Hee University, Korea
[2] Department of Mathematics, Yonsei University, Korea

E-mail: ejwoo@khu.ac.kr

Abstract

We describe a new multi-frequency technique for breast cancer detection. Applying a constant voltage with multiple sinusoidal frequencies between a reference electrode on a distal part of a patient and a scan probe placed on the breast, we measure exit currents from an array of electrodes inside the probe that are kept at the ground potential. The distribution of measured exit currents is called the trans-admittance map and the instrument is called the trans-admittance scanner (TAS). We assume a three-dimensional homogeneous domain including an internal lesion with a complex conductivity different from that of the background. Mathematically analyzing the multi-frequency trans-admittance map obtained on the surface of the domain, we found that both conductivity and permittivity ratios between the background and the lesion are crucial in extracting any useful information about the lesion from the map. Choosing two frequencies in the range of 10 Hz to 500 kHz with one significantly lower than the other and assuming that conductivity values of the background and the lesion do not change much from the low to high frequency, the lesion underneath the probe can be detected only when the conductivity ratio between the background and the lesion is different from the permittivity ratio between the background and the lesion at the chosen high frequency. Results of numerical simulations and saline phantom experiments using a developed TAS system are well matched with the mathematical analysis. The biggest advantage of this multi-frequency technique is that we do not need separately measured reference data in the absence of any lesion. We suggest future studies of a more sophisticated lesion detection algorithm based on the analysis and findings described in this paper.

(Some figures in this article are in colour only in the electronic version)

1. Introduction

Bioimpedance techniques such as electrical impedance tomography (EIT) have been suggested as a diagnostic tool for breast cancer detection. This is based on experimental findings showing that there exists a high contrast in the complex conductivity between cancerous and normal breast tissues (Surowiec *et al* 1988, Jossinet and Schmitt 1999, Silva *et al* 2000, Hartov *et al* 2005). For example, Kerner *et al* (2002) used circular arrays of electrodes around the breast and produced cross-sectional conductivity images using an EIT image reconstruction technique. Cherepenin *et al* (2001, 2002) adopted a planar array of 256 electrodes placed on the breast and sequentially injected currents between chosen pairs of electrodes and measured the induced voltage data on other electrodes. Using this kind of boundary measurements, they reconstructed three-dimensional EIT images of the breast called electrical impedance mammograms. There are also several investigations for the usefulness of a planar array of electrodes in EIT imaging of the breast (Larson-Wiseman 1998, Mueller *et al* 1999, Kao *et al* 2003). These approaches are to find lesions from cross-sectional EIT images. In this case, cancerous lesions within the breast should appear in the reconstructed EIT images.

On the other hand, there has been a different approach where feature extraction of lesions inside the breast is emphasized instead of the cross-sectional imaging. Figure 1(a) shows a configuration for breast cancer detection based on this kind of approach. A patient holds a reference electrode with one hand through which a constant voltage is applied. A scan probe is placed on the breast and it is equipped with a planar array of electrodes kept at the ground potential. The voltage difference produces current flows from the hand-held electrode to each grounded electrode of the scan probe through the breast. By measuring exit currents from all electrodes of the scan probe, we can obtain a two-dimensional trans-admittance map and extract some information on the complex conductivity distribution within the breast region under the probe. Basically, it has the same architecture as the early frontal plane impedance camera suggested by Henderson and Webster (1978).

Based on this configuration, a commercial system called T-Scan has been introduced for adjunctive clinical uses with x-ray mammography (Assenheimer *et al* 2001). Use of T-Scan is to decrease equivocal findings and thereby reduce unnecessary biopsies. However, the diagnostic information from the currently available T-Scan system lacks a sophisticated reconstruction method of finding lesions even though there were some clever works and observations in processing the trans-admittance data (Assenheimer *et al* 2001, Scholz 2002). Lately, Seo *et al* (2004) and Ammari *et al* (2004) studied this measurement configuration and developed a mathematical framework to analyze the trans-admittance data. Based on the framework, they derived a direct relation between lesions and trans-admittance data and suggested a non-iterative algorithm to extract core features of lesions.

A major drawback of the method is the requirement of reference trans-admittance data that were acquired in the absence of a lesion. Even though some statistical methods may be devised to replace the reference data, it is highly desirable to eliminate the use of the reference data in order to make the method more practical. To deal with this problem,
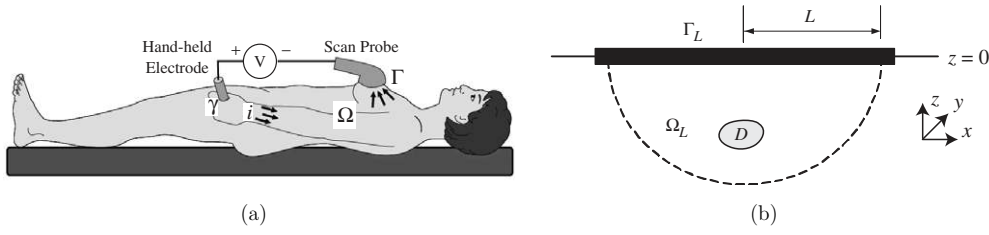
Figure 1. (a) Voltage is applied between the hand-held electrode and the planar array of electrodes in the scan probe. Exit currents through the scan probe are measured to provide trans-admittance data. (b) Simplified model of the breast region with a cancerous lesion D under the scan probe.

we pay attention to the multi-frequency technique which relies on any difference in trans-admittance maps simultaneously obtained at two or more different frequencies. Considering the complex conductivity distribution of the breast including both conductivity and permittivity, we should first correctly understand how it affects the trans-admittance map comprising real and imaginary parts. In this paper, we provide a mathematical analysis of the problem and describe the relationship between the complex conductivity and the frequency-difference trans-admittance map.

By showing results of numerical simulations and phantom experiments, we will discuss the possibility of lesion detection using multi-frequency trans-admittance maps. For the experimental works, we will use a developed multi-frequency trans-admittance scanner (TAS) that captures trans-admittance maps under the scan probe with 320 planar array of electrodes in the frequency range of 10 Hz to 500 kHz. We will briefly describe the design of the system that is based on a multi-frequency EIT system (Oh *et al* 2006). Analyzing numerical and experimental results, future improvements in the lesion estimation algorithm are suggested.

2. Methods

2.1. Problem definition

Let the human body shown in figure 1(a) occupy a three-dimensional domain Ω bounded by its surface $\partial\Omega$. Suppose that a constant voltage of a_0 in volt with an angular frequency ω is applied to the hand-held electrode denoted as γ. The contact area of the scan probe on the breast is denoted as Γ. The resulting complex voltage $V(\mathbf{r})$ at position $\mathbf{r} = (x, y, z)$ in Ω satisfies the following mixed boundary value problem:

$$\begin{cases} \nabla \cdot ((\sigma + i\omega\epsilon)\nabla V(\mathbf{r})) = 0, & \mathbf{r} \in \Omega \\ V(\mathbf{r}) = 0, & \mathbf{r} \in \Gamma \\ V(\mathbf{r}) = a_0, & \mathbf{r} \in \gamma \\ (\sigma + i\omega\epsilon)\nabla V(\mathbf{r}) \cdot \mathbf{n}(\mathbf{r}) = 0, & \mathbf{r} \in \partial\Omega \backslash (\Gamma \cup \gamma) \end{cases} \quad (1)$$

where $\mathbf{n}$ is the unit outward normal vector to the boundary, $\sigma = \sigma(\mathbf{r}, \omega)$ the conductivity and $\epsilon = \epsilon(\mathbf{r}, \omega)$ the permittivity. Both σ and ϵ depend on $\mathbf{r}$ and ω. Denoting the real and imaginary parts of V by $v = \mathrm{Re}\, V$ and $h = \mathrm{Im}\, V$, we have the following coupled system:

$$\begin{cases} \nabla \cdot (\sigma \nabla v) - \nabla \cdot (\omega\epsilon \nabla h) = 0 & \text{in } \Omega \\ \nabla \cdot (\omega\epsilon \nabla v) + \nabla \cdot (\sigma \nabla h) = 0 & \text{in } \Omega \\ v = 0 \quad \text{and} \quad h = 0 & \text{on } \Gamma \\ v = 1 \quad \text{and} \quad h = 0 & \text{on } \gamma \\ \mathbf{n} \cdot \nabla v = 0 \quad \text{and} \quad \mathbf{n} \cdot \nabla h = 0 & \text{on } \partial\Omega \backslash (\Gamma \cup \gamma). \end{cases} \quad (2)$$

In order to detect a lesion underneath the scan probe, we define a local region of interest under the probe plane Γ as shown in figure 1(b). For simplicity, we let z be the axis normal to Γ and let the center of Γ be the origin $\mathbf{0} = (0, 0, 0)$. Let L be the radius of the scan probe so that the two-dimensional probe region Γ_L is defined as

$$\Gamma_L := \left\{ (x, y, 0) : \sqrt{x^2 + y^2} < L \right\}. \tag{3}$$

We set the region of interest inside the breast as the half ball Ω_L shown in figure 1(b):

$$\Omega_L := \{ (x, y, z) : z < 0 \text{ and } \sqrt{x^2 + y^2 + z^2} < L \}. \tag{4}$$

The scan probe has a planar array of electrodes to measure the distribution of exit currents through Γ_L, that is, we measure

$$-g(\mathbf{r}) := \underbrace{\mathbf{n} \cdot (\sigma \nabla v - \omega \epsilon \nabla h)}_{\text{real part}} + \mathrm{i} \underbrace{\mathbf{n} \cdot (\sigma \nabla h + \omega \epsilon \nabla v))}_{\text{imaginary part}}, \qquad \mathbf{r} \in \Gamma_L. \tag{5}$$

In this paper, the distribution of exit currents g is called the trans-admittance map.

We suppose that there is a cancerous lesion D inside Ω_L as shown in figure 1(b). The complex conductivity $\tau := (\sigma + \mathrm{i}\omega\epsilon)$ changes abruptly across the interface ∂D and we assume

$$\tau := \sigma + \mathrm{i}\omega\epsilon = \begin{cases} \sigma^n + \mathrm{i}\omega\epsilon^n & \text{in the normal tissue } \Omega_L \setminus \bar{D} \\ \sigma^c + \mathrm{i}\omega\epsilon^c & \text{in the cancerous lesion } D. \end{cases} \tag{6}$$

Both trans-admittance maps g_1 and g_2 are simultaneously acquired at two different frequencies ω_1 and ω_2, respectively, from the breast region Ω_L with a lesion D.

2.2. Analysis of frequency-difference trans-admittance maps

We let $V_1 = v_1 + \mathrm{i}h_1$ and $V_2 = v_2 + \mathrm{i}h_2$ satisfying (2) at two different frequencies ω_1 and ω_2, respectively. Corresponding trans-admittance maps are denoted as g_1 and g_2, respectively. In practice, we may set $100 < \omega_1/2\pi < 500$ kHz and $\omega_2/2\pi < 1$ kHz. We assume that the corresponding complex conductivities are

$$\tau_j := \sigma_j + \mathrm{i}\omega_j\epsilon_j = \begin{cases} \tau_j^n := \sigma_j^n + \mathrm{i}\omega_j\epsilon_j^n & \text{in } \Omega_L \setminus \bar{D} \\ \tau_j^c := \sigma_j^c + \mathrm{i}\omega_j\epsilon_j^c & \text{in } D. \end{cases} \quad (j = 1, 2) \tag{7}$$

The following identity will provide a relation between the anomaly D and the frequency-difference trans-admittance map.

Proposition 2.1. *For any constant α, we have*

$$\int_\Gamma [g_1 - \alpha g_2] \, \mathrm{d}A = \frac{1}{a_0} \int_\Omega (\tau_1 - \alpha\tau_2) \nabla V_2 \cdot \nabla V_1 \, \mathrm{d}\mathbf{r} \tag{8}$$

where $\mathrm{d}A$ is the surface area element and $\mathrm{d}\mathbf{r}$ the volume element.

Proof. Since $\int_\Gamma g_j \, \mathrm{d}A = -\int_\gamma g_j \, \mathrm{d}A$ and $V_j = a_0$ on γ,

$$\int_\Gamma [g_1 - \alpha g_2] \, \mathrm{d}A = \int_\gamma [\alpha g_2 - g_1] \, \mathrm{d}A = \frac{1}{a_0} \int_\gamma [\alpha g_2 V_1 - g_1 V_2] \, \mathrm{d}A.$$

Using the boundary conditions that are $V_j = 0$ on Γ_L and $g_j = 0$ on $\partial\Omega \setminus \overline{\Gamma_L \cup \gamma}$,

$$\frac{1}{a_0} \int_\gamma [\alpha g_2 V_1 - g_1 V_2] \, \mathrm{d}A = \frac{1}{a_0} \int_{\partial\Omega} [\alpha g_2 V_1 - V_2 g_1] \, \mathrm{d}A.$$

According to the divergence theorem,

$$\frac{1}{a_0} \int_{\partial\Omega} [\alpha g_2 V_1 - V_2 g_1] \, \mathrm{d}A = \frac{1}{a_0} \int_\Omega (\tau_1 - \alpha\tau_2) \nabla V_2 \cdot \nabla V_1 \, \mathrm{d}\mathbf{r}.$$

Then, (8) follows from the above three identities. □

Formula (8) provides an interesting relation between the anomaly D and the Neumann data or trans-admittance maps g_1, g_2 on Γ of the simplified model. Suppose that complex conductivities $\sigma_j^n + i\omega_j\epsilon_j^n$ (in the normal tissue) and $\sigma_j^c + i\omega_j\epsilon_j^c$ (in the cancerous tissue) are constants. Substituting $\alpha = \frac{\sigma_1^n + i\omega_1\epsilon_1^n}{\sigma_2^n + i\omega_2\epsilon_2^n}$ into (8) yields

$$\int_{\Gamma} \left[g_1 - \left(\frac{\sigma_1^n + i\omega_1\epsilon_1^n}{\sigma_2^n + i\omega_2\epsilon_2^n} \right) g_2 \right] dA = \frac{\eta_1[\omega_1, \omega_2]}{a_0} \int_D \nabla V_2 \cdot \nabla V_1 \, d\mathbf{r} \tag{9}$$

where

$$\eta_1[\omega_1, \omega_2] := \left[\left(\sigma_1^c + i\omega_1\epsilon_1^c \right) - \left(\frac{\sigma_1^n + i\omega_1\epsilon_1^n}{\sigma_2^n + i\omega_2\epsilon_2^n} \right) \left(\sigma_2^c + i\omega_2\epsilon_2^c \right) \right]. \tag{10}$$

Now, we examine whether the multi-frequency trans-admittance map can provide any information of the anomaly D even though the frequency dependency of conductivity σ is very small from ω_1 to ω_2. To be precise, we assume that the conductivity and permittivity at ω_1 and ω_2 satisfy the followings:

 (i) We choose two frequencies ω_1 and ω_2 with $\omega_2 \ll \omega_1$ so that $\frac{\omega_2\epsilon^n}{\sigma_2^n} \approx 0$ and $\frac{\omega_2}{\omega_1} \approx 0$.
 (ii) We assume that there are negligibly small changes in conductivities from ω_2 to ω_1, that is, $\sigma_1^n = \sigma_2^n = \sigma^n$ and $\sigma_1^c = \sigma_2^c = \sigma^c$.

Observation 2.2. *The weighted difference between two trans-admittance maps at ω_1 and ω_2 provides the following information of the anomaly D:*

$$\int_{\Gamma} \left[g_1 - \left(\frac{\sigma^n + i\omega_1\epsilon_1^n}{\sigma^n + i\omega_2\epsilon_2^n} \right) g_2 \right] dA \approx i\frac{\omega_1\epsilon_1^n}{a_0} \left[\frac{\epsilon_1^c}{\epsilon_1^n} - \frac{\sigma^c}{\sigma^n} \right] \int_D \nabla V_2 \cdot \nabla V_1 \, d\mathbf{r}. \tag{11}$$

Hence, we can detect D from the multi-frequency trans-admittance map as long as $\frac{\epsilon_1^c}{\epsilon_1^n} \neq \frac{\sigma^c}{\sigma^n}$.

Proof. From conditions (i) and (ii), the value of $\eta_1[\omega_1, \omega_2]$ in (10) becomes

$$\eta_1[\omega_1, \omega_2] = \left[\left(\sigma^c + i\omega_1\epsilon_1^c \right) - \left(\frac{\sigma^n + i\omega_1\epsilon_1^n}{\sigma^n + i\omega_2\epsilon_2^n} \right) \left(\sigma^c + i\omega_2\epsilon_2^c \right) \right]$$

$$= i\left(\omega_1\epsilon_1^c - \omega_2\epsilon_2^c \right) + \left(1 - \frac{\sigma^n + i\omega_1\epsilon_1^n}{\sigma^n + i\omega_2\epsilon_2^n} \right) \left(\sigma^c + i\omega_2\epsilon_2^c \right)$$

$$= i\left(\omega_1\epsilon_1^c - \omega_2\epsilon_2^c \right) + \frac{1}{\sigma^n + i\omega_2\epsilon_2^n} \left[i\sigma^c \left(\omega_2\epsilon_2^n - \omega_1\epsilon_1^n \right) - \omega_2\epsilon_2^c \left(\omega_2\epsilon_2^n - \omega_1\epsilon_1^n \right) \right]$$

$$\approx i\omega_1\epsilon_1^n \left[\frac{\epsilon_1^c}{\epsilon_1^n} - \frac{\sigma^c}{\sigma^n} \right].$$

Therefore, the identity (9) becomes

$$\int_{\Gamma} \left[g_1 - \left(\frac{\sigma^n + i\omega_1\epsilon_1^n}{\sigma^n + i\omega_2\epsilon_2^n} \right) g_2 \right] dA \approx i\frac{\omega_1\epsilon_1^n}{a_0} \left[\frac{\epsilon_1^c}{\epsilon_1^n} - \frac{\sigma^c}{\sigma^n} \right] \int_D \nabla V_2 \cdot \nabla V_1 \, d\mathbf{r}. \tag{12}$$

$\square$

The above observation shows that the lesion detection is possible from the frequency-difference trans-admittance map $g_1 - \alpha g_2$ with an appropriate choice of α provided that $\frac{\epsilon_1^c}{\epsilon_1^n} \neq \frac{\sigma^c}{\sigma^n}$. On the other hand, if $\frac{\epsilon_1^c}{\epsilon_1^n} = \frac{\sigma^c}{\sigma^n}$, it is impossible to detect the lesion from the frequency-difference trans-admittance map. In practice, the condition of $\frac{\epsilon_1^c}{\epsilon_1^n} = \frac{\sigma^c}{\sigma^n}$ seldom occurs primarily due to the heterogeneity of tissues even though the difference $\frac{\epsilon_1^c}{\epsilon_1^n} - \frac{\sigma^c}{\sigma^n}$ could be small in some case.

2.3. Numerical simulation method

In order to numerically test the observation in (12), we considered a cubic model $\Omega := [0, 0.08] \times [0, 0.08] \times [0, 0.08]$ m^3 and set the probe region $\Gamma := \{(x, y, 0.08) : \sqrt{(x - 0.04)^2 + (y - 0.04)^2} < 0.03\}$ where we computed trans-admittance maps. We assumed that $\Omega \backslash D$ is homogeneous and $\sigma^n, \sigma^c, \epsilon_1^n, \epsilon_2^n, \epsilon_1^c, \epsilon_2^c$ are constants. We set $\sigma^n = 0.1$ S m^{-1} and $\frac{\sigma^c}{\sigma^n} = 5$. For permittivity values, we set $\epsilon_1^n = 50 \times 8.854 \times 10^{-12}$ F m^{-1}, $\epsilon_2^n = 100 \times 8.854 \times 10^{-12}$ F m^{-1}, $\frac{\epsilon_1^c}{\epsilon_1^n} = 10$ and $\frac{\epsilon_2^c}{\epsilon_2^n} = 20$. We used FEM by discretizing the cubic model Ω with $40 \times 40 \times 40$ hexahedral elements to solve the following mixed boundary value problem:

$$\begin{cases} \nabla \cdot ((\sigma + i\omega\epsilon)\nabla V(\mathbf{r})) = 0, & \mathbf{r} \in \Omega \\ V(\mathbf{r}) = 0, & \mathbf{r} \in \Gamma \\ V(x, y, 0) = 1 & \text{for } x, y \in [0, 0.08] \\ (\sigma + i\omega\epsilon)\nabla V(\mathbf{r}) \cdot \mathbf{n}(\mathbf{r}) = 0, & \mathbf{r} \in \partial\Omega \backslash (\Gamma \cup \{z = 0\}). \end{cases} \quad (13)$$

We computed numerical solutions of (13) at two different frequencies of $f_1 = \omega_1/2\pi = 200$ kHz and $f_2 = \omega_2/2\pi = 500$ Hz for a cube-shaped anomaly D with its side length of 0.004 m at the center of $(0.04, 0.04, 0.07)$ in metres. We varied the size and location of the anomaly and repeated numerical computations. For the choice of frequencies, we fixed f_2 at 500 Hz and varied f_1 as 50 and 100 kHz.

For a quantitative estimation of the anomaly D, we defined

$$Y_{D,\omega_1,\omega_2} = \frac{1}{\omega_1 \epsilon_1^n} \int_\Gamma \left[g_1 - \left(\frac{\sigma^n + i\omega_1 \epsilon_1^n}{\sigma^n + i\omega_2 \epsilon_2^n} \right) g_2 \right] \mathrm{d}A. \quad (14)$$

From (11), the above identity (14) can be approximated by

$$Y_{D,\omega_1,\omega_2} \approx i \left[\frac{\epsilon_1^c}{\epsilon_1^n} - \frac{\sigma^c}{\sigma^n} \right] \int_D \nabla V_2 \cdot \nabla V_1 \, \mathrm{d}\mathbf{r}.$$

Therefore, we can see that the imaginary part of $g_1 - \left(\frac{\sigma^n + i\omega_1 \epsilon_1^n}{\sigma^n + i\omega_2 \epsilon_2^n}\right) g_2$, the integrand of the left-hand side in (12), plays a key role in the detection of the anomaly for the case where there is little frequency dependency in conductivities.

2.4. TAS system and experimental method

For the experimental testing, we used a multi-frequency TAS system shown in figure 2 including the following parts: (i) PC with USB port and TAS software, (ii) main controller with USB interface, (iii) intra-network controller, (iv) constant sinusoidal voltage source, (v) multiple ammeters, (vi) hand-held electrode, (vii) scan probe with planar array of electrodes and switches and (viii) dc power supply. The TAS system shares most parts with the multi-frequency EIT system developed by Oh *et al* (2006).

2.4.1. Constant voltage source. The constant voltage source consists of an FPGA, 16-bit DAC, 8-bit DAC and operational amplifier. Sixteen-bit data of a quarter period of the normalized sinusoid are stored in the FPGA and an address generator outputs the data to the 16-bit DAC. We implemented the address generator such that the sinusoidal frequency can be varied by a command from the main controller. We can choose a frequency in the range of 10 Hz to 500 kHz. We can scale the amplitude of the voltage signal at the 16-bit DAC output from 0 to 2.5 V by properly setting the 8-bit DAC. In this way, we generate a sinusoidal voltage signal with a variable amplitude and frequency.
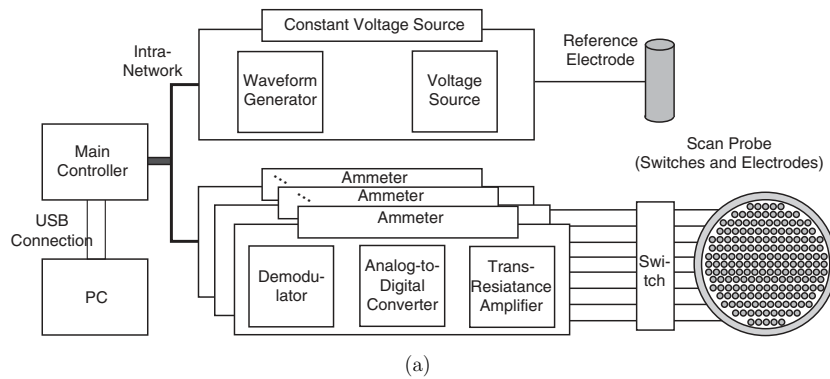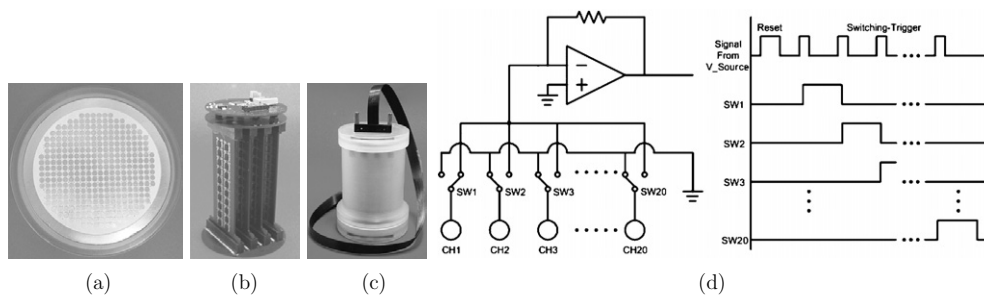
(a)
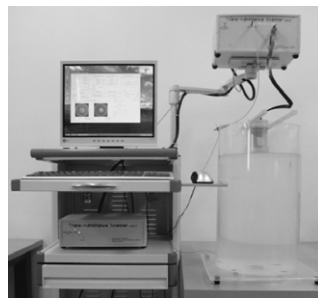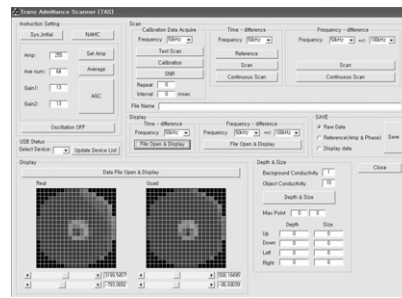
(b)   (c)

Figure 2. (a) Block diagram and (b) picture of the developed TAS system. (c) Screen capture of the TAS software.

(a)   (b)   (c)   (d)

Figure 3. Scan probe with switches and 320 gold-coated array electrodes: (a) bottom view, (b) side view and (c) assembled probe. (d) Schematic diagram of switching circuit inside the probe.

2.4.2. Hand-held electrode and scan probe with planar array of electrodes. The hand-held electrode is a simple copper cylinder connected to the constant voltage source. Figures 3(a)–(c) show the manufactured scan probe with 320 gold-coated array electrodes. Each array electrode is circular with a diameter of 2 mm and the effective contact area of 320 electrodes is 3318.3 mm^2. The planar array of electrodes is enclosed by a guard electrode in a shape of a ring with its surface area of 1099.6 mm^2.
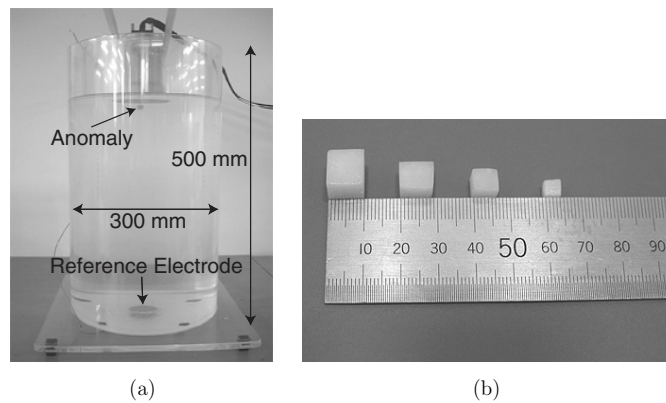
Figure 4. (a) Saline phantom with an anomaly. A disc-shaped reference electrode is placed at the bottom of the phantom. (b) Anomalies with different sizes.

2.4.3. Ammeter. There are 16 ammeters and each ammeter is sequentially connected to one of a set of 20 current-sensing electrodes. The front-end of each ammeter is a trans-resistance amplifier that converts the exit current from a selected electrode to the amplified voltage signal. Each array electrode in the scan probe is switched either to the circuit ground or to a chosen trans-resistance amplifier as shown in figure 3(d). The trans-resistance amplifier is a simple current-to-voltage converter with the connected electrode virtually grounded (Franco 2002). The output can be further amplified with a variable gain voltage amplifier. Using a 12-bit ADC at 10 MHz sampling frequency, we quantize the amplified voltage signal and feed the digital data to the FPGA for the subsequent digital phase-sensitive demodulation. For the demodulation, the method described by Cook *et al* (1994) was implemented in the FPGA. The demodulator outputs are real (in-phase) and imaginary (quadrature) parts of the complex trans-admittance from a chosen current-sensing electrode in the scan probe.

2.4.4. Calibration and saline phantom experiments. We used a resistor phantom to calibrate each ammeter for different gains and frequencies. We usually use 32 different gains from a total 65 536 possible gains. For the multi-frequency operation, we may choose several frequencies from 4096 possible frequencies in the range of 10 Hz to 500 kHz.

2.4.5. Experimental settings. Figure 4(a) shows a saline tank with 0.39 S m^{-1} conductivity. Inside the tank, we placed an anomaly of 0.68 S m^{-1}. Figure 4(b) shows anomalies with different sizes made of TX151 (Oil Center Research International, Lafayette, LA, USA), NaCl and sucrose (Mazzara *et al* 1996). We obtained two trans-admittance data sets g_1 and g_2 at two different frequencies of ω_1 and ω_2, respectively. During these experiments, we changed the size and depth of the anomaly. The low frequency $f_2 = \omega_2/2\pi$ was fixed at 500 Hz and the high frequency $f_1 = \omega_1/2\pi$ was varied with three different values of 50, 100 and 200 kHz.

3. Results

3.1. Numerical simulation results

Figure 5 shows a typical numerical solution of (13) at $f_1 = 200$ kHz. In the plots, solid lines are equipotential lines of V_1 and arrows indicate the direction and magnitude of electric
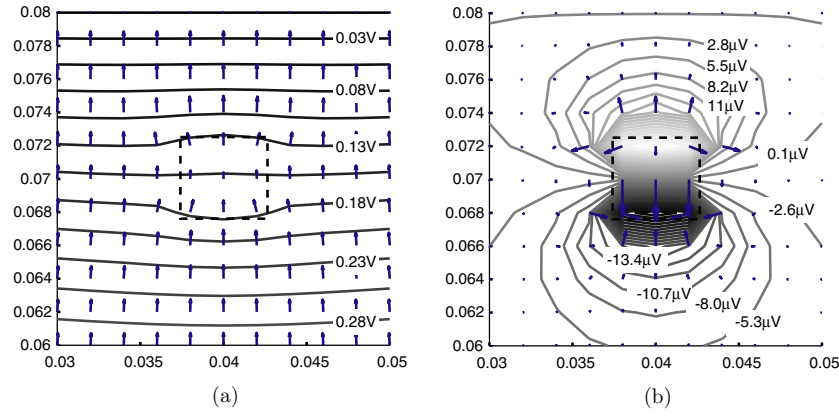
Figure 5. Equipotential lines of V_1 and electric field $-\nabla V_1$ at $f_1 = 200$ kHz in the slice $\{(x, y, z) : x = 0.04, 0.03 < y < 0.05, 0.06 < z < 0.08\}$. Arrows indicate the magnitude and direction of $-\nabla V_1$. The anomaly D was a cube-shaped domain with its side length of 0.004 m at the center of $(0.04, 0.04, 0.07)$ in metres. (a) Real and (b) imaginary parts of V_1 and $-\nabla V_1$.
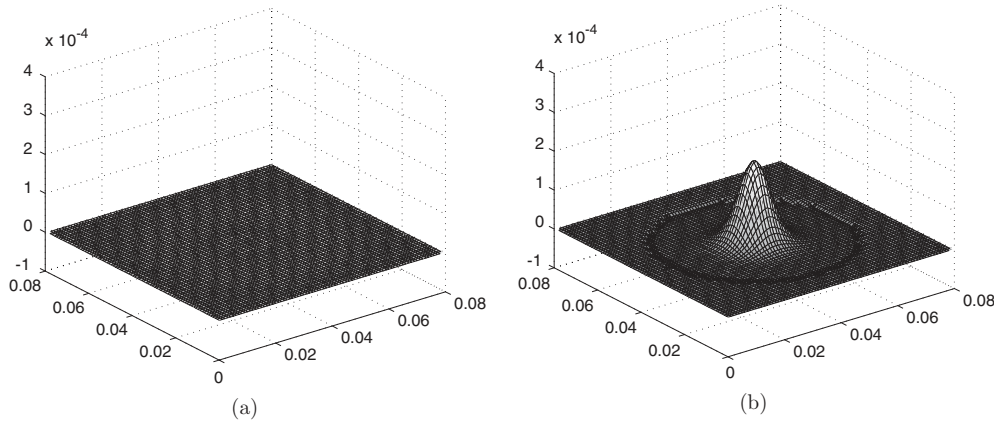

Figure 6. Frequency-difference trans-admittance map: (a) real and (b) imaginary parts of $(g_1 - \alpha g_2)$ with $f_1 = \omega_1/2\pi = 200$ kHz and $f_2 = \omega_2/2\pi = 500$ Hz.

field $-\nabla V_1$. Figure 6 shows the real and imaginary parts of the trans-admittance map $g_1 - \alpha g_2$ with $f_1 = 200$ kHz and $f_2 = 500$ Hz. As expected, the imaginary part of $g_1 - \alpha g_2$ clearly shows the existence of the anomaly D for this case where conductivities did not change with frequency.

Table 1 shows a summary of many numerical simulations using different sizes and depths of D and three different values of $f_1 = 50, 100$ and 200 kHz for a fixed $f_2 = 500$ Hz. The side length of D was either 4 or 8 mm and the depth was 8, 16 or 24 mm. As expected, the imaginary part of Y_{D,ω_1,ω_2} is consistent and provides a core information of D.

3.2. Saline phantom experiment results

Figures 7 and 8 show imaginary parts of the measured trans-admittance map $g_1 - \alpha g_2$ with $f_1 = 200$ kHz and $f_2 = 500$ Hz for an anomaly with different sizes and depths. We can observe that the peak value and slope of the map are influenced by the size and depth of the

Table 1. Summary of numerical simulations showing that the imaginary part of Y_{D,ω_1,ω_2}, $\mathrm{Im}\{Y_{D,\omega_1,\omega_2}\}$, contains a core information of D. The low frequency was $f_2 = \omega_2/2\pi = 500$ Hz.

Frequency ratio ω_1/ω_2	Size (mm^3)	Depth (mm)	$Y_{D,\omega_1,\omega_2} \times 10^6$ Imaginary part	Real part	$\mathrm{Im}\{Y_{D,\omega_1,\omega_2}\}/|D|$
100	4^3	8	23.70	−9.42	370.28
200	4^3	8	24.46	0.54	382.20
400	4^3	8	24.84	0.90	388.16
100	4^3	16	17.29	53.36	270.18
200	4^3	16	17.85	26.86	278.88
400	4^3	16	18.13	−22.74	283.23
100	4^3	24	12.67	−27.48	198.02
200	4^3	24	13.08	−1.77	204.43
400	4^3	24	13.29	2.91	207.63
100	8^3	8	164.00	−20.83	320.32
200	8^3	8	169.24	−9.51	330.55
400	8^3	8	171.86	9.49	335.66
100	8^3	16	117.16	20.45	228.82
200	8^3	16	120.90	9.31	236.13
400	8^3	16	122.77	−1.48	239.78
100	8^3	24	87.59	−91.90	171.08
200	8^3	24	90.39	8.97	176.54
400	8^3	24	91.79	4.93	179.27

anomaly. In figure 7, where we fixed the depth of the anomaly, the peak value increases as the anomaly size is increased. Figure 8 illustrates that the peak value decreases as the depth is increased when the size is fixed. The decrease becomes significant when the depth was 15 and 20 mm.

For all measured trans-admittance maps using the TAS system, we computed Y_{D,ω_1,ω_2} in (14) and summarized the results in table 2. As in table 1, the imaginary part of Y_{D,ω_1,ω_2} is consistent providing information of D. However, in table 2, we can see that the real part also shows similar consistency and provides information of D. We believe that this is related with frequency dependency of conductivity.

4. Discussion and conclusion

When we try to utilize a TAS system for breast cancer detection, we should take advantage of a difference imaging scheme. This is primarily to cancel out numerous unknown factors and preserve the information on the anomaly that has a different complex conductivity value compared with those of the surrounding background tissues. Considering the fact that there is very little chance to be provided with a measured trans-admittance map in the absence of an anomaly, we have investigated the frequency-difference technique in this paper.

We chose the frequency range from 10 Hz to 500 kHz mainly because the measurement error in our TAS system rapidly increases beyond 500 kHz. At this relatively low frequency range, almost all previous works in EIT have assumed that $\omega\epsilon/\sigma$ is negligible. However, this assumption seems to be invalid for most biological tissues and we should consider
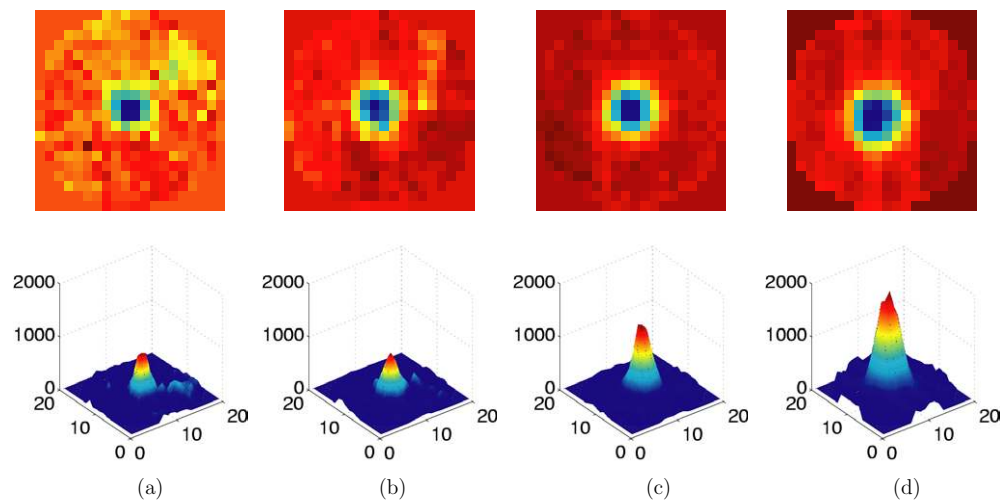
Figure 7. Imaginary part of $g_1 - \alpha g_2$ from the saline phantom in figure 4 with a cubic anomaly at 5 mm depth with four different side lengths of (a) 4, (b) 6, (c) 8 and (d) 10 mm. Two-dimensional plots are individually scaled and three-dimensional plots are shown by using the same scale. We used two different frequencies of $f_1 = 200$ kHz and $f_2 = 500$ Hz.

Figure 8. Imaginary part of $g_1 - \alpha g_2$ from the saline phantom in figure 4 with a cubic anomaly with its side length of 10 mm at four different depths of (a) 5, (b) 10, (c) 15 and (d) 20 mm. Two-dimensional plots are individually scaled and three-dimensional plots are shown by using the same scale. We used two different frequencies of $f_1 = 200$ kHz and $f_2 = 500$ Hz.
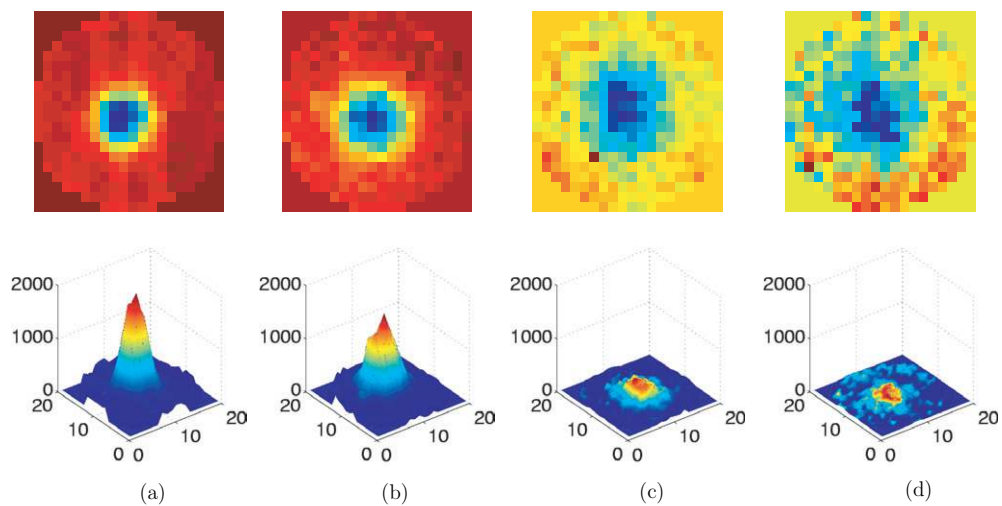
both conductivity and permittivity when we try to utilize a frequency-difference technique. We would like to emphasize that the coupled system in (2) must be the starting point for the analysis and algorithm development in multi-frequency works including the frequency-difference imaging method in EIT as well as the lesion detection in TAS described in this paper.

Table 2. Computed values of $\mathrm{Im}\{Y_{D,\omega_1,\omega_2}\}/|D|$ from measured trans-admittance maps using the TAS system and saline phantom. Mean $\pm$ standard deviation from five repeated measurements. The low frequency was $f_2 = \omega_2/2\pi = 500$ Hz.

Frequency ratio ω_1/ω_2	Size (mm^3)	Depth (mm)	$Y_{D,\omega_1,\omega_2} \times 10^9$		$\mathrm{Im}\{Y_{D,\omega_1,\omega_2}\}/|D|$
			Imaginary part	Real part	
100	4^3	5	190.49 ± 12.04	-84.35 ± 6.27	2.976 ± 0.188
200	4^3	5	192.16 ± 10.75	-83.35 ± 8.44	3.002 ± 0.168
400	4^3	5	179.97 ± 8.93	-35.49 ± 18.80	2.812 ± 0.139
100	6^3	5	95.03 ± 2.89	-164.35 ± 16.57	0.440 ± 0.013
200	6^3	5	98.11 ± 3.06	-160.62 ± 20.85	0.454 ± 0.014
400	6^3	5	101.97 ± 2.84	-154.83 ± 14.51	0.472 ± 0.013
100	8^3	5	133.50 ± 11.31	-217.04 ± 9.61	0.261 ± 0.022
200	8^3	5	148.64 ± 11.26	-231.55 ± 11.13	0.290 ± 0.022
400	8^3	5	171.29 ± 10.85	-213.36 ± 15.91	0.335 ± 0.021
100	10^3	5	627.16 ± 43.16	-574.07 ± 41.73	0.627 ± 0.043
200	10^3	5	639.96 ± 42.09	-587.01 ± 39.91	0.640 ± 0.042
400	10^3	5	616.37 ± 36.99	-566.50 ± 28.28	0.616 ± 0.037
100	10^3	10	403.66 ± 15.46	-456.04 ± 18.44	0.404 ± 0.015
200	10^3	10	441.91 ± 14.89	-464.06 ± 17.84	0.442 ± 0.015
400	10^3	10	513.12 ± 13.96	$-464.50 \pm 14, 43$	0.513 ± 0.014
100	10^3	15	113.87 ± 9.80	-132.99 ± 32.90	0.114 ± 0.010
200	10^3	15	119.83 ± 10.50	-115.59 ± 14.80	0.120 ± 0.011
400	10^3	15	128.36 ± 9.41	-91.95 ± 16.88	0.128 ± 0.009
100	10^3	20	-5.95 ± 1.78	-38.19 ± 0.61	-0.006 ± 0.002
200	10^3	20	-4.37 ± 1.76	-33.94 ± 10.57	-0.004 ± 0.002
400	10^3	20	-7.72 ± 1.68	-33.85 ± 2.46	-0.008 ± 0.002

As far as we know, there have been few studies on (13) including both conductivity σ and permittivity ϵ. As illustrated in figure 5(a), the real parts of computed complex voltage V and electric field $-\nabla V$ show expected behavior. On the other hand, the imaginary parts in figure 5(b) show interesting patterns with both positive and negative voltages. In this specific numerical example, we can observe that the direction of imaginary part of electric field changes on some boundary of the anomaly. More rigorous mathematical and numerical analyses on these imaginary parts are needed for better understanding of the complex conductivity problem in (13).

Trying to detect an anomaly from a frequency-difference trans-admittance map, the computed maps in figure 6 indicate that we should focus on its imaginary part if the conductivity ratio between the background and the lesion is relatively independent of the frequency. If this condition is not applicable, however, we should investigate both real and imaginary parts. In figure 6(b), we can readily observe that the transversal position of the anomaly is easy to be estimated as the peak position of the map. In this paper showing the feasibility of the frequency-difference method, we used the simple parameter of $\mathrm{Im}\{Y_{D,\omega_1,\omega_2}\}/|D|$ to extract some information about the anomaly. From table 1, we can see that the computed values of $\mathrm{Im}\{Y_{D,\omega_1,\omega_2}\}/|D|$ clearly distinguish the anomaly with different sizes and depths. However, this parameter alone is not enough to estimate its size and depth separately since the effects

of both size and depth are mixed in the value of $\text{Im}\{Y_{D,\omega_1,\omega_2}\}/|D|$. In terms of the choice of frequency, we can observe that the computed values of $\text{Im}\{Y_{D,\omega_1,\omega_2}\}/|D|$ are not sensitive to the frequency ratio used in the simulation.

The measured frequency-difference trans-admittance maps in figures 7 and 8 have similar patterns to the computed map in figure 6(b). The measured maps show that the peak value and width of the elevation change with the size and depth of the anomaly. This should be utilized in our future study of an anomaly estimation algorithm. The computed values of the parameter $\text{Im}\{Y_{D,\omega_1,\omega_2}\}/|D|$ in table 2 using measured maps show similar results to the numerical simulations summarized in table 1.

The last three rows in table 2 indicate that the present TAS system does not have enough accuracy to detect the anomaly at the depth of 20 mm. In terms of the hardware performance, we plan to improve the signal-to-noise ratio (SNR) in measured trans-admittance data since it will be the ultimate limiting factor in detecting an anomaly with a small size and large depth. The spatial resolution of measured trans-admittance maps is basically limited by the number and size of the current-sensing electrode. With 320 electrodes, we speculate that the spatial resolution is not the major part of future improvements since we can move the scan probe over the breast slowly.

Results of numerical simulations and saline phantom experiments clearly show the feasibility of a frequency-difference method of detecting a lesion using a TAS system with 10 Hz to 500 kHz bandwidth. Our major future work will be the development of a new algorithm that provides robust estimates of anomaly size and location from single or multiple frequency-difference trans-admittance maps. This will require a very rigorous mathematical analysis of the coupled system in (2). Though Seo *et al* (2004) and Ammari *et al* (2004) developed such a lesion estimation algorithm, it was primarily for a time-difference method and is not suitable for a frequency-difference method.

Acknowledgment

References

Ammari H, Kwon O, Seo J K and Woo E J 2004 T-Scan electrical impedance imaging system for anomaly detection *SIAM J. Appl. Math.* **65** 252–66

Assenheimer M, Laver-Moskovitz O, Malonek D, Manor D, Nahliel U, Nitzan R and Saad A 2001 The T-Scan technology: electrical impedance as a diagnostic tool for breast cancer detection *Physiol. Meas.* **22** 1–8

Cherepenin V, Karpov A, Korjenevsky A, Kornienko V, Kultiasov Y, Ochapkin M, Trochanova O and Meister J 2002 Three-dimensional EIT imaging of breast tissues: system design and clinical testing *IEEE Trans. Med. Imag.* **21** 662–7

Cherepenin V, Karpov A, Korjenevsky A, Kornienko V, Mazaletskaya A, Mazourov D and Meister J 2001 A 3D electrical impedance tomography (EIT) system for breast cancer detection *Physiol. Meas.* **22** 9–18

Cook R D, Saulnier G J, Gisser D G, Goble J G, Newell J C and Isaacson D 1994 ACT3: a high-speed, high-precision electrical impedance tomography *IEEE Trans. Biomed. Eng.* **41** 713–22

Franco S 2002 *Design with Operational Amplifiers and Analog Integrated Circuits* 3rd edn (New York: McGraw-Hill)

Hartov A, Soni N and Halter R 2005 Breast cancer screening with electrical impedance tomography *Electrical Impedance Tomography: Methods, History and Applications* ed D S Holder (Bristol: Institute of Physics Publishing)

Henderson R P and Webster J G 1978 An impedance camera for spatially specific measurements of the thorax *IEEE Trans. Biomed. Eng.* **25** 250–4

Jossinet J and Schmitt M 1999 A review of parameters for the bioelectrical characterization of breast tissue *Ann. N. Y. Acad. Sci.* **873** 30–41

Kao T, Newell J C, Saulinier G J and Isaacson D 2003 Distinguishability of inhomogeneities using planar electrode arrays and different patterns of applied excitation *Physiol. Meas.* **24** 403–11

Kerner T E, Paulsen K D, Hartov A, Soho S K and Poplack S P 2002 Electrical impedance spectroscopy of the breast: clinical imaging results in 26 subjects *IEEE Trans. Med. Imag.* **21** 638–45

Larson-Wiseman J L 1998 Early breast cancer detection utilizing clustered electrode arrays in impedance imaging *PhD Thesis* RPI, Troy, NY, USA

Mazzara G P, Briggs R W, Wu Z and Steinbach B G 1996 Use of a modified polysaccharide gel in developing a realistic breast phantom for MRI *Mag. Res. Imag.* **14** 639–48

Mueller J L, Isaacson D and Newell J C 1999 A reconstruction algorithm for electrical impedance tomography data collected on rectangular electrode arrays *IEEE Trans. Biomed. Eng.* **46** 1379–86

Oh T I, Woo E J and Holder D 2007 Multi-frequency EIT system with radially symmetric architecture: KHU Mark1 *Physiol. Meas.* **28** S183–96

Scholz B 2002 Towards virtual electrical breast biopsy: space-frequency MUSIC for trans-admittance data *IEEE Trans. Med. Imag.* **21** 588–95

Seo J K, Kwon O, Ammari H and Woo E J 2004 Mathematical framework and anomaly estimation algorithm for breast cancer detection: electrical impedance technique using TS2000 configuration *IEEE Trans. Biomed. Eng.* **51** 1898–906

Silva J E, Marques J P and Jossinet J 2000 Classification of breast tissue by electrical impedance spectroscopy *Med. Biol. Eng. Comput.* **38** 26–30

Surowiec A J, Stuchly S S, Barr J R and Swarup A 1988 Dielectric properties of breast carcinoma and the surrounding tissues *IEEE Trans. Biomed. Eng.* **35** 257–63